



Kinetic-scale Current Sheets in the Solar Wind at 1 au: Properties and the Necessary Condition for Reconnection

I. Y. Vasko^{1,2} , K. Alimov¹, T. D. Phan¹ , S. D. Bale^{1,3} , F. S. Mozer¹ , and A. V. Artemyev^{2,4}

¹Space Sciences Laboratory, University of California at Berkeley, USA; vaskoiy@berkeley.edu

²Space Research Institute of Russian Academy of Sciences, Moscow, Russia

³Department of Physics, University of California at Berkeley, USA

⁴University of California, Los Angeles, USA

Received 2021 October 29; revised 2021 November 29; accepted 2021 December 1; published 2021 December 14

Abstract

We present a data set and properties of 18,785 proton kinetic-scale current sheets collected over 124 days in the solar wind using magnetic field measurements at 1/11 s resolution aboard the Wind spacecraft. We show that all of the current sheets are in the parameter range where reconnection is not suppressed by diamagnetic drift of the X-line. We argue this necessary condition for magnetic reconnection is automatically satisfied due to the geometry of current sheets dictated by their source, which is the local plasma turbulence. The current sheets are shown to be elongated along the background magnetic field and dependence of the current sheet geometry on local plasma beta is revealed. We conclude that reconnection in the solar wind is not likely to be suppressed or controlled by the diamagnetic suppression condition.

Unified Astronomy Thesaurus concepts: [Solar wind \(1534\)](#); [Solar magnetic reconnection \(1504\)](#); [Interplanetary turbulence \(830\)](#)

1. Introduction

Current sheets (CS) in the solar wind were identified aboard early spacecraft missions as variations of the magnetic field direction over timescales less than a few tens of seconds (Burlaga et al. 1977; Tsurutani & Smith 1979; Lepping & Behannon 1986). A substantial number of studies were focused on classifying CSs in terms of tangential and rotational MHD discontinuities, but did not provide consistent results (e.g., Neugebauer 2006). The multispacecraft studies showed that the methodology used in these single-spacecraft studies is typically incapable of accurately estimating the normal to a CS surface, which explains the contradictory classifications (Horbury et al. 2001; Knetter et al. 2004; Artemyev et al. 2019). In previous studies, CSs were selected using magnetic field measurements at a few second resolution at best, which corresponds to ≈ 1000 km spatial resolution. The typical occurrence rate of the CSs at 1 au was about a few tens per day, while the typical thickness was around ten proton inertial lengths. The analysis of magnetic field measurements at 1/3 s resolution by Vasquez et al. (2007) demonstrated that CSs with a thickness of a few proton inertial lengths are much more abundant with typical occurrence rates of a few hundred CSs per day. Vasquez et al. (2007) also suggested that kinetic-scale CSs are highly likely produced by solar wind turbulence, which was further supported by Greco et al. (2009, 2016) and Zhdankin et al. (2012).

Observations of reconnecting CSs in the solar wind have been reported fairly recently (Gosling et al. 2005, 2007; Gosling 2007, 2012). Based on 3 s resolution of plasma measurements (≈ 1000 km spatial resolution), magnetic reconnection is relatively rare, about one reconnecting CS per day (Gosling 2012). Observations showed that plasma heating

does occur around current sheets in the solar wind (Osman et al. 2011; Wu et al. 2013) and magnetic reconnection indeed contributes to the plasma heating (Phan et al. 2006; Enži et al. 2014; Pulupa et al. 2014; Mistry et al. 2017), but its net contribution is still not known because the occurrence of reconnection at proton kinetic scales and conditions controlling reconnection onset are not entirely understood (Phan et al. 2010, 2020; Gosling & Phan 2013; Osman et al. 2014). In this Letter we present analysis of a condition that was previously considered crucial for reconnection onset in solar wind CSs.

Theory and simulations showed that magnetic reconnection in a planar CS with magnetic shear angle $\Delta\theta$ (angle between magnetic fields at the CS boundaries) and plasma beta variation $\Delta\beta$ across the boundaries is allowed/suppressed if the following condition is satisfied/violated (Swisdak et al. 2003, 2010)

$$\Delta\beta \lesssim 2(L/\lambda_p)\tan(\Delta\theta/2), \quad (1)$$

where L is the spatial scale of the plasma pressure gradient across the X-line and λ_p is the proton inertial length. If condition (1) is violated, magnetic reconnection is suppressed because diamagnetic drift of the X-line exceeds characteristic Alfvén speeds. Thus, condition (1) is necessary, though not sufficient, for magnetic reconnection to occur. Phan et al. (2010) collected about 200 reconnecting CSs in the solar wind at 1 au and showed that condition (1) is indeed satisfied by all of them provided that L/λ_p is on the order of one. The latter assumption, in turn, is consistent with the fact that magnetic reconnection is sufficiently fast only in CSs with thickness comparable to ion inertial length (e.g., Cassak et al. 2006). Phan et al. (2020) have recently considered about 20 reconnecting CSs observed at 0.2 au aboard the Parker Solar Probe and found that all of them satisfy condition (1). These reports, along with a few others (Gosling & Phan 2013; Phan et al. 2013), could create an impression that condition (1)

determines reconnection onset in solar wind CSs, although Phan et al. (2020) noted that about 50 nonreconnecting CSs also satisfied condition (1).

In this Letter we present a data set of 18,785 proton kinetic-scale CSs and demonstrate that condition (1) is almost always satisfied by kinetic-scale CSs in the solar wind. We show it is automatically satisfied due to the geometry of the CSs, dictated by their source, which is the local plasma turbulence. Thus, reconnection in the solar wind cannot be suppressed or controlled by the diamagnetic suppression condition.

2. Data and Methods

We use measurements of the Wind spacecraft which is located at the L1 Lagrangian point, about 200 Earth radii from the Earth. The magnetic field measurements at 1/11 s resolution are provided by the Magnetic Field Instrument (Lepping et al. 1995); proton densities, flow velocities, and temperatures at 3 s cadence are provided by the Wind 3DP instrument (Lin et al. 1995); and electron densities and temperatures at about 9 s cadence are provided by the Solar Wind Experiment instrument (Ogilvie et al. 1995). Note that proton densities coincide with electron densities within a few tens of percent. We consider a period of 124 days, from 2010 October 1 to 2011 February 2 except the first 16 hr on 2010 December 7, when magnetic field data at 1/11 s resolution were not available.

CSs were selected using the partial variance increment (PVI) method (e.g., Greco et al. 2018). The original method is based on computing PVI index, $PVI(t, \tau) = |\Delta \mathbf{B}(t, \tau)| / \sigma$, where $\Delta \mathbf{B}(t, \tau) = \mathbf{B}(t + \tau) - \mathbf{B}(t)$ are magnetic field increments, while σ is the standard deviation of $\Delta \mathbf{B}(t, \tau)$ computed over a sufficiently long time interval. Coherent structures at various temporal scales correspond to non-Gaussian fluctuations with, for example, $PVI > 5$. We used another PVI index, $PVI = (\sum_{\alpha} \Delta B_{\alpha}^2(t, \tau) / \sigma_{\alpha}^2)^{1/2}$, which allows selecting more coherent structures, because each component of $\Delta \mathbf{B}(t, \tau)$ is normalized by its standard deviation σ_{α} , rather than by $\sigma = [\sum_{\alpha} \sigma_{\alpha}^2]^{1/2}$, where $\alpha = X, Y, Z$. We computed standard deviations over 2 hr intervals, that is, over a few outer correlation scales of solar wind turbulence (Matthaeus et al. 2005). We used only the PVI index computed at $\tau = 1/11$ s to focus on the thinnest resolvable coherent structures.

To select CSs among the non-Gaussian fluctuations, each of about $2 \cdot 10^5$ continuous clusters of points with $PVI > 5$ was considered over intervals of ± 1 s, ± 2 s, ± 3 s, and ± 4 s around its center and magnetic field component $\mathbf{B} \cdot \mathbf{x}'$ was computed, where \mathbf{x}' is a unit vector along the direction of maximum magnetic field variation computed using the maximum variance analysis method (e.g., Sonnerup & Scheible 1998). We visually inspected all profiles of $\mathbf{B} \cdot \mathbf{x}'$ and selected clusters of points with $\mathbf{B} \cdot \mathbf{x}'$ reversing the sign within at least one of the intervals. We then manually adjusted the boundaries so that each boundary had a duration of at least half a second and excluded events with substantial relative variations of the magnetic field at the boundaries. The CSs were classified into nonbifurcated and bifurcated, the latter type characterized by $\mathbf{x}' \cdot d\mathbf{B}/dt$ with two well-separated peaks and often observed in reconnection exhausts (e.g., Gosling 2012). A short temporal duration of the CSs did not allow establishing the presence or absence of reconnection plasma jets and, thus, we could not determine the fraction of reconnecting CSs.

The final data set includes 18,785 CSs with 1742 of them classified as bifurcated. Each CS is considered in a local coordinate system \mathbf{xyz} most suitable for describing CS structure (Knetter et al. 2004; Gosling & Phan 2013; Phan et al. 2020); unit vector \mathbf{z} is along the CS normal determined by the cross product of magnetic field vectors at the CS boundaries; unit vector \mathbf{x} is along $\mathbf{x}' - \mathbf{z} \cdot (\mathbf{x}' \cdot \mathbf{z})$; unit vector \mathbf{y} completes the right-handed coordinate system, $\mathbf{y} = \mathbf{z} \times \mathbf{x}$. Note that the conclusions of this study will be independent of the local coordinate system used to describe the CSs and of our visual classification.

To determine the variation of plasma beta across a CS, we assume there is a pressure balance, $8\pi P + B^2 = 8\pi\Pi = \text{const}$ or $8\pi P/B^2 + 1 = 8\pi\Pi/B^2$, where P is the thermal plasma pressure. There are one or two points of proton measurements and one point of electron measurements around each CS, so that constant parameter Π can be computed by averaging the pressure balance across the CS, $\Pi = \langle B^2 \rangle / 8\pi + \langle P \rangle$ and $8\pi\Pi \langle 1/B^2 \rangle = \langle 8\pi P/B^2 \rangle + 1$, where the spatial averaging of plasma pressure is equivalent to time-averaging done by the Wind plasma instruments. The variation of plasma beta can then be determined as follows

$$\Delta\beta \approx (1 + \beta)\Delta(B^{-2})/\langle B^{-2} \rangle, \quad (2)$$

where $\beta = \langle 8\pi P/B^2 \rangle = (8\pi\langle P \rangle + \langle B^2 \rangle)\langle B^{-2} \rangle - 1$ is the averaged plasma beta, and $\Delta(B^{-2})$ is the variation of $1/B^2$ across the CS. Equation (2) provides an approximate estimate of the plasma beta variation across the CS, because the exact value of this quantity could be determined using only particle measurements at the CS boundaries as has been done, for example, for rather wide reconnection exhausts (Phan et al. 2010). The relatively low cadence of plasma measurements does not allow us to determine the plasma beta variation using plasma measurements because in our data set, magnetic fields at the CS boundaries may substantially vary on a timescale of 3–9 s. Nevertheless, we found that a blind use of particle measurements about 9 s before and after the CSs provided similar, though not equivalent, values of $\Delta\beta$, such that the use of these $\Delta\beta$ values would not change any of our conclusions.

3. Overview and Case Studies

Figure 1 presents an overview of Wind spacecraft measurements. Panels (a)–(d) present 2 hr averaged magnetic field magnitude, proton and electron densities, proton flow velocity, and proton and electron temperatures. The considered interval of 124 days corresponds to about four solar rotation periods and we consistently observe periodic variations of proton moments. The faster (slower) solar wind is more tenuous (dense) and carries a hotter (colder) proton population. The electron temperature does not vary with solar rotation and remains around 15 eV. All the features in panels (a)–(d) are consistent with the classical structure of the solar wind at 1 au (e.g., Newbury et al. 1998; Cranmer et al. 2017).

Panel (e) presents a percentage of fluctuations, that is a relative number of magnetic field increments $\Delta \mathbf{B}(t, \tau)$, with $PVI > 5$ computed every 2 hr. The averaged percentage of fluctuations with $PVI > 5$ is about 0.5%, that is four orders of magnitude larger than one would observe if magnetic field increments $\Delta \mathbf{B}(t, \tau)$ had a Gaussian probability distribution. This is in accordance with previous observations that magnetic field increments in the solar wind have probability distributions

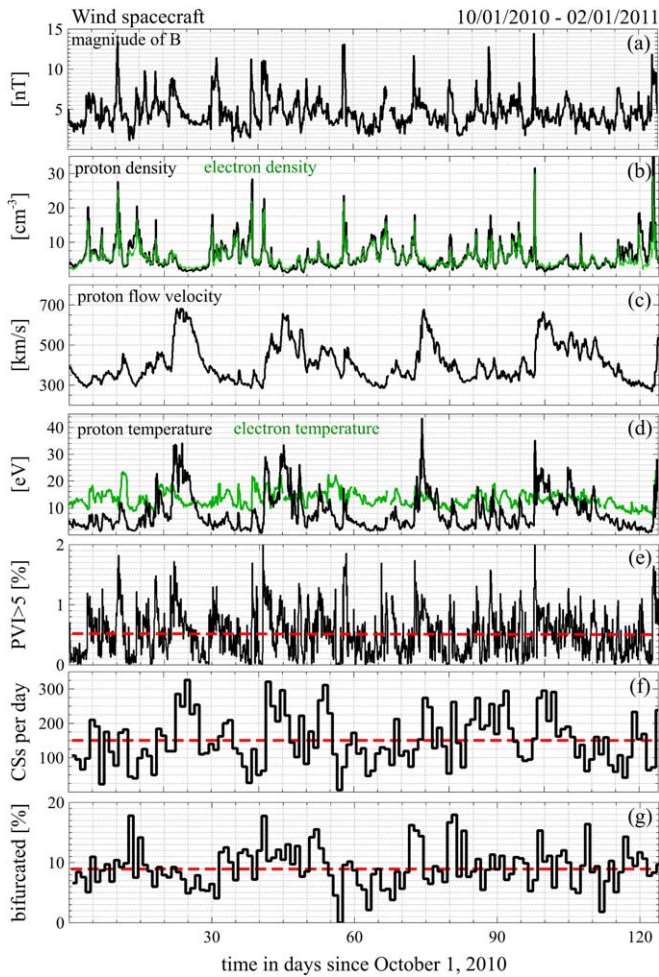


Figure 1. Overview of Wind spacecraft measurements over 124 days, from 2010 October 1 to 2011 February 2. Panels (a)–(d) present 2 hr averaged magnetic field magnitude, proton and electron densities, proton flow velocity, and proton and electron temperatures. Panel (e) presents the percentage of fluctuations with PVI index larger than 5. Note that in the case of magnetic field increments with a Gaussian probability distribution the percentage of fluctuations with PVI > 5 would be less than $10^{-4}\%$. Panel (f) shows the number of current sheets (CSs) per day, while panel (g) demonstrates the occurrence rate of bifurcated CSs in percents with respect to total number of CSs per day. The red dashed lines in panels (e)–(g) represent the averaged (over 124 days) values of the corresponding quantities.

with heavy non-Gaussian tails (e.g., Sorriso-Valvo et al. 1999; Greco et al. 2018). Panel (e) shows that the percentage of the non-Gaussian fluctuations varies substantially over time in the range from about 0.01% to 2%. The local bursts in the percentage of the non-Gaussian fluctuations are always associated with local increases of the magnetic field magnitude and plasma density and often with local increases of proton temperature.

Panel (f) presents the number of CSs per day selected in the considered interval. The occurrence rate varies from about 10 to 320 CSs per day, while the averaged occurrence rate is about 150 CSs per day. These occurrence rates are consistent with those of CSs resolved at 1/3 s magnetic field resolution (Vasquez et al. 2007). The local increases in the number of CSs are often, though not always, associated with local bursts in the percentage of the non-Gaussian fluctuations. Panel (g) shows that the averaged occurrence rate of bifurcated CSs is around 9%.

Figure 2 presents several CSs from our data set. The left panels show a nonbifurcated CS. Panel (a) presents magnetic field magnitude and three magnetic field components in the Geocentric Solar Ecliptic coordinate system. The magnetic field rotates across the CS through shear angle $\Delta\theta \approx 117^\circ$, while the magnitude varies from about 0.5 to 1.6 nT. We define the averaged magnetic field magnitude $\langle B \rangle$ as the half sum of magnetic field magnitudes at the CS boundaries, and variation ΔB as the absolute value of their difference. For the considered CS, we have $\langle B \rangle \approx 1.05$ nT and $\Delta B \approx 1.1$ nT. The CS is observed in a plasma with local proton density of 11 cm^{-3} , proton temperature of 2 eV, and electron temperature of 10 eV, so that averaged plasma beta is rather high, $\beta \approx 108$. The variation of plasma beta across the CS is even larger, $\Delta\beta \approx 160$, because it is dominated by beta at the boundary with a smaller magnetic field magnitude. Such large values of β and $\Delta\beta$ are actually not typical of solar wind CSs, but we demonstrate this CS to show that $\Delta B/\langle B \rangle$ can be on the order of one.

Panel (b) presents the magnetic field in the local CS coordinate system xyz . The magnetic field component B_x varies from about 0.5 to -1.5 nT, while B_y is more or less constant across the CS. The magnetic field component B_z is around zero at the CS boundaries in accordance with the definition of the CS normal and remains small within the CS. We characterize the asymmetry of a CS by $\langle B_x \rangle$, which is the half sum of B_x values at the CS boundaries and the CS amplitude by the absolute value of their difference denoted as ΔB_x . The guide field will be characterized by B_g which is the half sum of B_y values at the CS boundaries. For the considered CS we have $\Delta B_x \approx 2$ nT, $\langle B_x \rangle \approx -0.5$ nT and $B_g \approx -0.5$ nT.

Panel (c) presents current densities J_x and J_y estimated as follows

$$J_y = -\frac{c}{4\pi V_n} \frac{dB_x}{dt}, \quad J_x = \frac{c}{4\pi V_n} \frac{dB_y}{dt}, \quad (3)$$

where V_n is the normal component of proton flow velocity at the moment closest to the CS. In Equation (3) we took into account that the Taylor frozen-in hypothesis is valid at spatial scales larger than electron kinetic scales (e.g., Chasapis et al. 2017). The spatial coordinate along the normal, $z = -\int V_n dt$, is shown in Figure 2. Note that in Equation (3) we assumed that the CS is locally one-dimensional, which is in accordance with previous multispacecraft observations (Knetter et al. 2004; Artemyev et al. 2019), so that $\partial B_z/\partial x$ and $\partial B_z/\partial y$ are negligible compared to $\partial B_x/\partial z$ and $\partial B_y/\partial z$. We estimate the CS thickness as follows

$$\lambda = \frac{c}{4\pi} \frac{\Delta B_x}{2\langle J_y \rangle}, \quad (4)$$

where $\langle J_y \rangle$ is the absolute value of current density J_y averaged over the CS central region, $|B_x - \langle B_x \rangle| < 0.2\Delta B_x$, highlighted in Figure 2. For the considered CS we have $\lambda \approx 130$ km.

Panel (d) presents current densities parallel and perpendicular to the local magnetic field computed as $J_{\parallel} = (J_x B_x + J_y B_y)/B$ and $J_{\perp} = (J_y B_x - J_x B_y)/B$. By noting that the local magnetic field of a CS can be described as $\mathbf{B} = B(z)\sin\theta(z)\mathbf{x} + B(z)\cos\theta(z)\mathbf{y} + B_z\mathbf{z}$, where $B_z \ll B(z)$, we

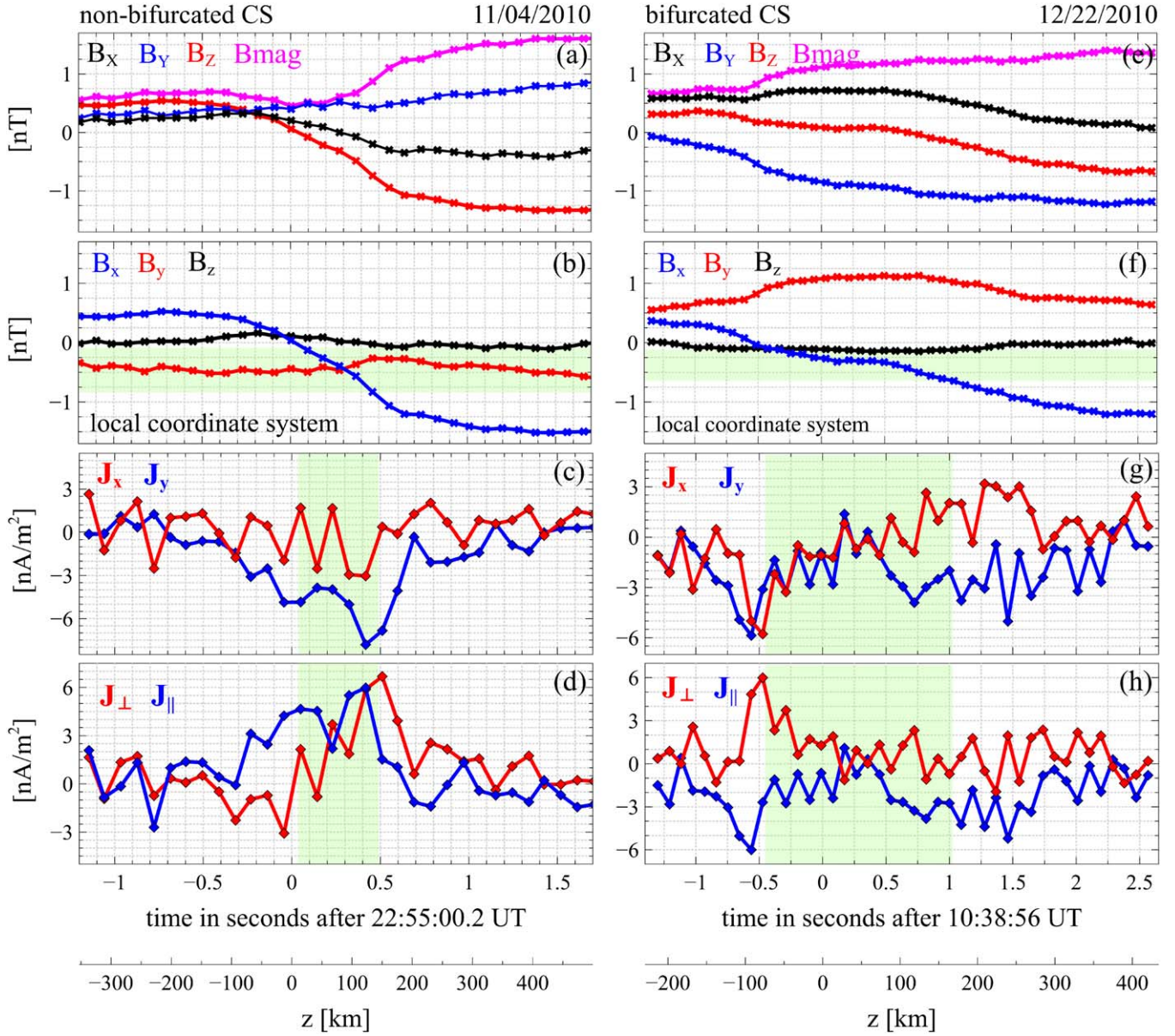


Figure 2. Examples of nonbifurcated (left panels) and bifurcated (right panels) current sheets from our data set: (a,e) magnetic field magnitude and three magnetic field components in the Geocentric Solar Ecliptic coordinate system; (b), (f) three magnetic field components in local coordinate system xyz defined in Section 2; (c), (g) current densities J_x and J_y estimated using Equation (3); (d), (h) current densities parallel and perpendicular to local magnetic field, $J_{\parallel} = (J_x B_x + J_y B_y)/B$ and $J_{\perp} = (J_y B_x - J_x B_y)/B$, where B is magnetic field magnitude. The bottom horizontal axes show the spatial coordinate across each CS, $z = -\int V_n dt$, where V_n is proton flow velocity along CS normal. The highlighted regions in panels (b)–(d) and (f)–(h) correspond to the CS central region, $|B_x - \langle B_x \rangle| < 0.2 \Delta B_x$, where $\langle B_x \rangle$ is the half sum of B_x values at the CS boundaries, while ΔB_x is the absolute values of their difference.

find that

$$J_{\parallel} = \frac{c}{4\pi} B \frac{d\theta}{dz}, \quad J_{\perp} = \frac{c}{4\pi} \frac{dB}{dz}. \quad (5)$$

Thus, the parallel and perpendicular current densities determine magnetic field rotation $\theta(z)$ and its magnitude variation $B(z)$ within CS, respectively.

Panels (e)–(h) present a bifurcated CS. The magnetic field rotates across the CS through shear angle $\Delta\theta \approx 90^\circ$, and the magnitude varies from 0.7 to 1.4 nT, so that $\langle B \rangle \approx 1$ nT and $\Delta B \approx 0.7$ nT. The CS is asymmetric with $\langle B_x \rangle \approx -0.4$ nT, amplitude $\Delta B_x \approx 1.6$ nT and guide field $B_g \approx 0.6$ nT. The local plasma has a density of 4 cm^{-3} , proton temperature of

3.2 eV, and electron temperature of 10.3 eV, so that $\beta \approx 21$ and $\Delta\beta \approx 39$. The intrinsic feature of this CS is that the parallel current density in panel (h) has a double-peaked profile and, correspondingly, magnetic field rotation occurs in two steps, with B_y increasing across the first step and decreasing across the second one. These are classical features of bifurcated CSs and reconnection exhausts in the solar wind (e.g., Gosling & Szabo 2008). We determined temporal duration of each bifurcated CS manually as a half of the temporal distance between centers of the two steps of magnetic field rotation. For the considered bifurcated CS, this duration is about 2.1 s, while the corresponding thickness is $\lambda \approx 170$ km.

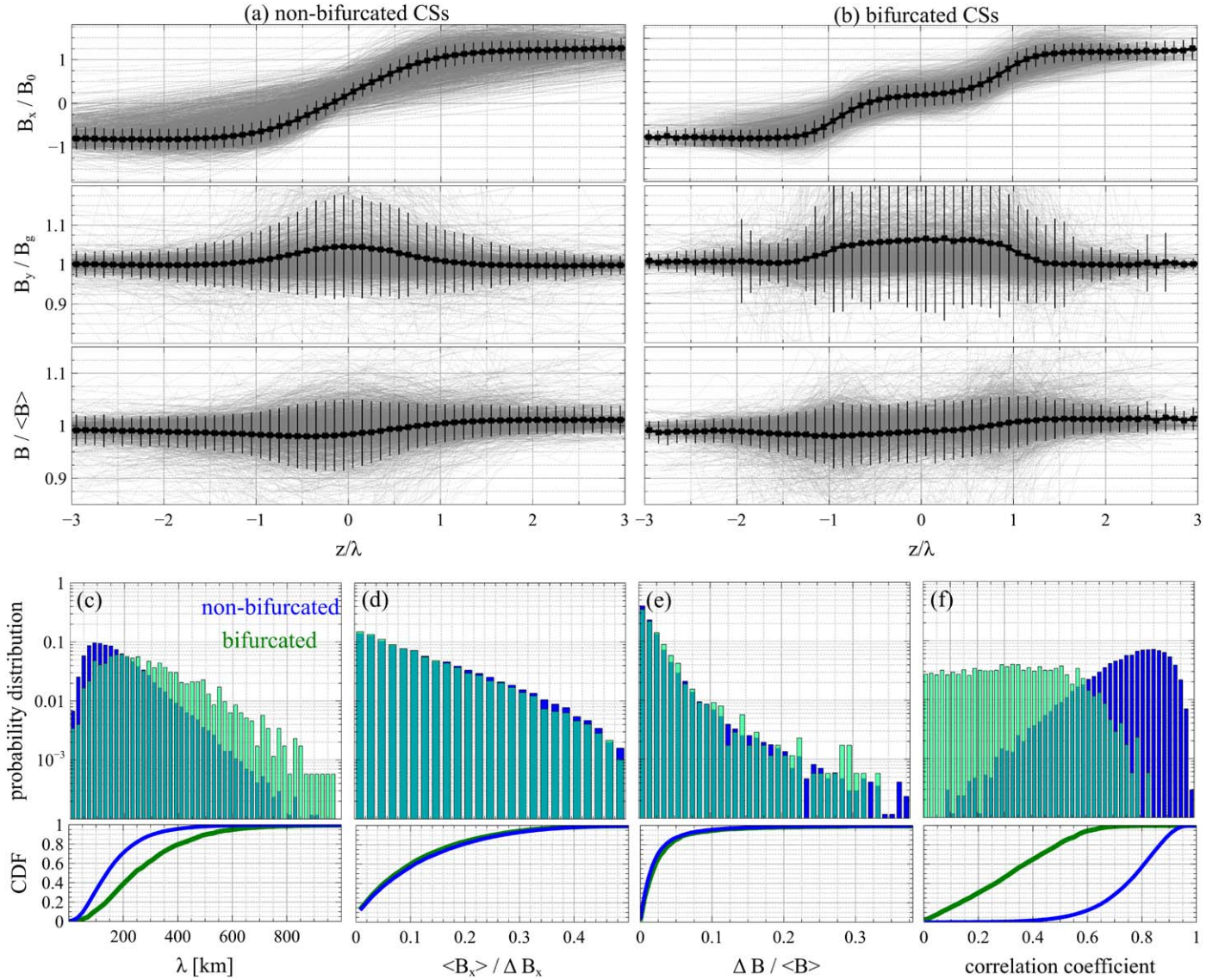


Figure 3. Averaged (black) and individual (gray) magnetic field profiles of (a) nonbifurcated and (b) bifurcated CSs. Individual profiles of B_x , B_y , and B were normalized respectively to $B_0 = 0.5\Delta B_x$, B_g , and $\langle B \rangle$, and then aligned by normalizing the spatial coordinate z to CS thickness λ and setting $z = 0$ at the CS center, where $z = 0$ corresponds to $B_x = \langle B_x \rangle$ for nonbifurcated CSs and to the center between the two steps of magnetic field rotation for bifurcated CSs. The error bars in panels (a) and (b) indicate the standard deviations of the averaged profiles. Panels (c)–(f) present probability distributions and corresponding cumulative distribution functions of various parameters for bifurcated and nonbifurcated CSs: CS thickness λ , asymmetry parameter $\langle B_x \rangle / \Delta B_x$, relative variation of magnetic field magnitude $\Delta B / \langle B \rangle$, and correlation coefficient between observed parallel current density J_{\parallel} and corresponding model profile of a nonbifurcated CS (see Section 4 for details).

4. Statistical Results

Figure 3 presents averaged profiles of various magnetic field components for bifurcated and nonbifurcated CSs. Before computing the averaged profiles, individual CS profiles were appropriately normalized and aligned. Individual profiles of B_x , B_y , and B were respectively normalized to $B_0 = 0.5\Delta B_x$, B_g , and $\langle B \rangle$. The CS profiles were aligned by normalizing spatial distance z to CS thickness λ and setting $z = 0$ at the CS center, where $z = 0$ corresponds to $B_x = \langle B_x \rangle$ for nonbifurcated CSs and to the center between the two steps of magnetic field rotation for bifurcated CSs. Note that we used a signed value of B_0 , so that B_x/B_0 is always negative at $z < 0$ and positive at $z > 0$. If the absolute value of a particular B_x/B_0 profile at the left boundary was larger than at the right boundary, this profile was reflected with respect to $z = 0$ and multiplied by -1 . The corresponding B_y/B_g and $B/\langle B \rangle$ profiles were reflected too.

This procedure allows us to keep the smaller of the boundary values of B_x/B_0 at $z < 0$.

Panels (a) and (b) present the normalized and aligned profiles of individual CSs along with the averaged profiles. The averaged profiles of B_x/B_0 show that both bifurcated and nonbifurcated CSs are typically asymmetric. The averaged profiles of B_y/B_g show that the guide field is statistically larger around the CS central region than at the CS boundaries, though only by a few percent. In contrast to B_x , the values of B_y at the different CS boundaries are statistically similar. The averaged profiles also show that magnetic field rotation occurs smoothly within nonbifurcated CSs, but in two steps within bifurcated CSs. By definition of the CS normal, B_z is zero around the CS boundaries and remains on average below $0.05\langle B \rangle$ within CS (not shown here). The averaged profiles of $B/\langle B \rangle$ show that the magnetic field magnitude varies by less than 5% within both nonbifurcated and bifurcated CSs. The magnetic field

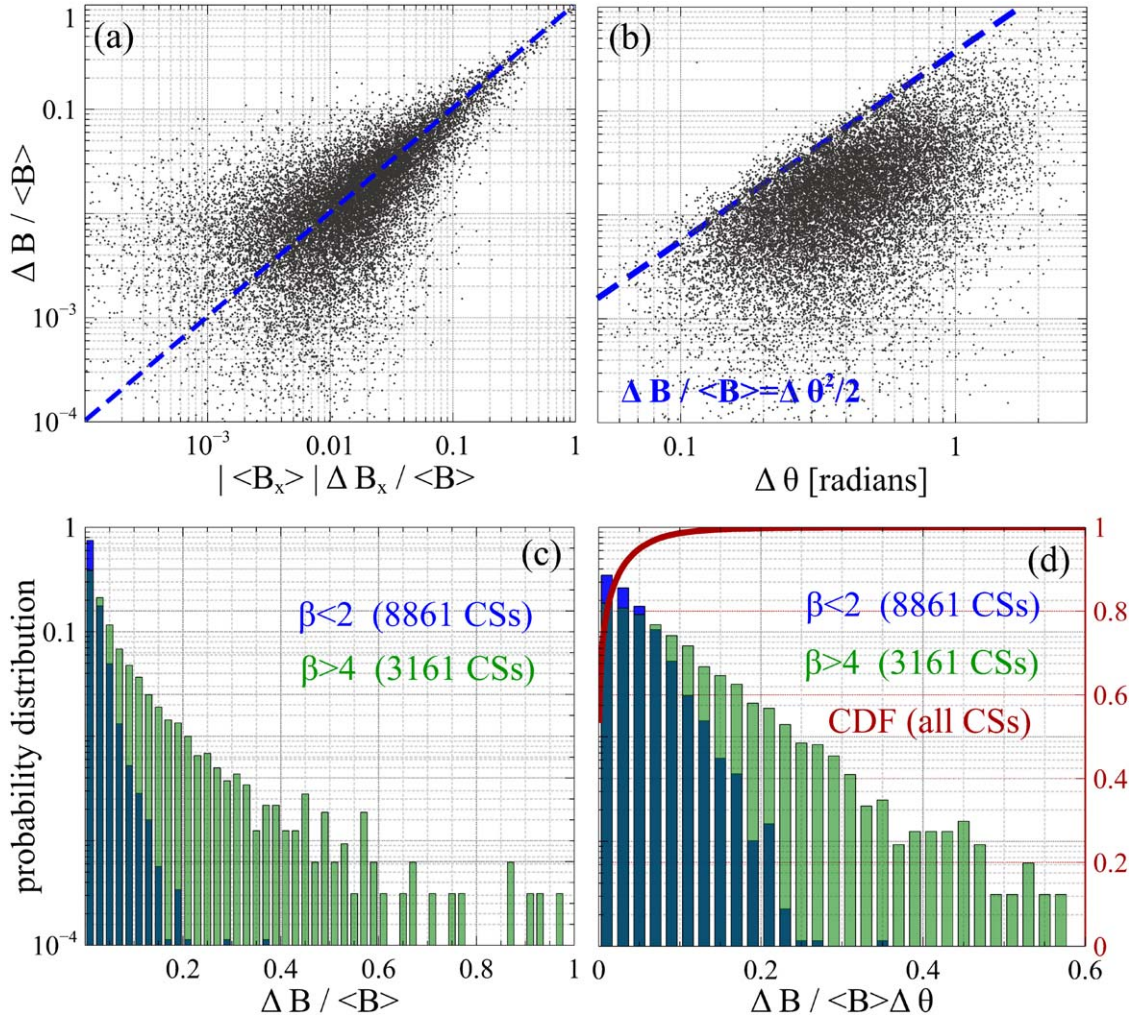


Figure 4. The scatter plots of (a) $\Delta B/\langle B \rangle$ vs. absolute value of $\langle B_x \rangle \Delta B_x / \langle B \rangle^2$ and (b) $\Delta B/\langle B \rangle$ vs. $\Delta \theta$, which are plotted to test predictions of Equation (6). Panels (c) and (d) present probability distributions of $\Delta B/\langle B \rangle$ and $\Delta B/\langle B \rangle \Delta \theta$ for CSs observed at $\beta < 2$ and $\beta > 4$. Panel (d) also presents the cumulative distribution function of $\Delta B/\langle B \rangle \Delta \theta$ for all CSs.

magnitude at the CS boundaries are statistically different by a few percent with the larger value at the right boundary. The averaged profiles indicate that the variation of the magnetic field magnitude across the CSs is statistically due to the B_x asymmetry, $\Delta(B^2) = \Delta(B_x^2) + \Delta(B_y^2) \approx \Delta(B_x^2)$, which can be rewritten as follows

$$\langle B \rangle \Delta B \approx \langle B_x \rangle \Delta B_x. \quad (6)$$

For example, the variations of the magnetic field magnitude across the CSs presented in Section 3 are due to the B_x asymmetry.

Panels (c)–(f) present probability distributions of several parameters of bifurcated and nonbifurcated CSs. Panel (c) shows that nonbifurcated CSs have thickness from a few tens to about 1000 km with the most probable value around 100 km. The bifurcated CSs have statistically larger thicknesses, but distributed in the same range. These spatial scales correspond to the range from a few tenths to ten proton inertial lengths and, thus, the considered CSs are proton kinetic-scale structures. Panels (d) and (e) show that both types of CSs are typically asymmetric with essentially identical distributions of $\langle B_x \rangle / \Delta B_x$ and $\Delta B/\langle B \rangle$. Panel (f) presents the probability distributions of the correlation coefficient between parallel current density J_{\parallel}

and model nonbifurcated profile $\langle J_{\parallel} \rangle \text{sech}^2(V_n t / \lambda)$, where λ was determined by Equation (4) for all CSs, $t = 0$ corresponds to $B_x = \langle B_x \rangle$ and $\langle J_{\parallel} \rangle$ is parallel current density averaged over the CS central region. The correlation coefficient is larger (smaller) than 0.55 for more than 90% of nonbifurcated (bifurcated) CSs, which proves adequacy of our visual classification of the CSs.

Figure 4 further addresses the cause of magnetic field variation across the CSs. Panel (a) shows that $\Delta B/\langle B \rangle$ is correlated with $\langle B_x \rangle \Delta B_x / \langle B \rangle^2$, especially at $\Delta B/\langle B \rangle \gtrsim 0.05$, so that sufficiently large magnetic field variations across the CSs are predominantly due to the B_x asymmetry. Equation (6) shows that we should observe $\Delta B/\langle B \rangle \lesssim \Delta \theta^2/2$, because $\langle B_x \rangle \lesssim \Delta B_x/2$ and $\Delta B_x \approx \langle B \rangle \Delta \theta$. Panel (b) confirms that $\Delta B/\langle B \rangle \lesssim \Delta \theta^2/2$ and also reveals positive correlation between $\Delta B/\langle B \rangle$ and $\Delta \theta$. Although $\Delta B/\langle B \rangle \lesssim 0.1$ for more than 95% of the CSs (Figure 3(e)), $\Delta B/\langle B \rangle$ can be rather large for individual CSs. Panels (c) and (d) present probability distributions of $\Delta B/\langle B \rangle$ and $\Delta B/\langle B \rangle \Delta \theta$ for CSs observed at $\beta < 2$ and $\beta > 4$ and show that larger values of these quantities are typically observed at higher betas. Accordingly, these quantities are atypically large for the two CSs considered in Section 3, because these CSs are observed at very high betas.

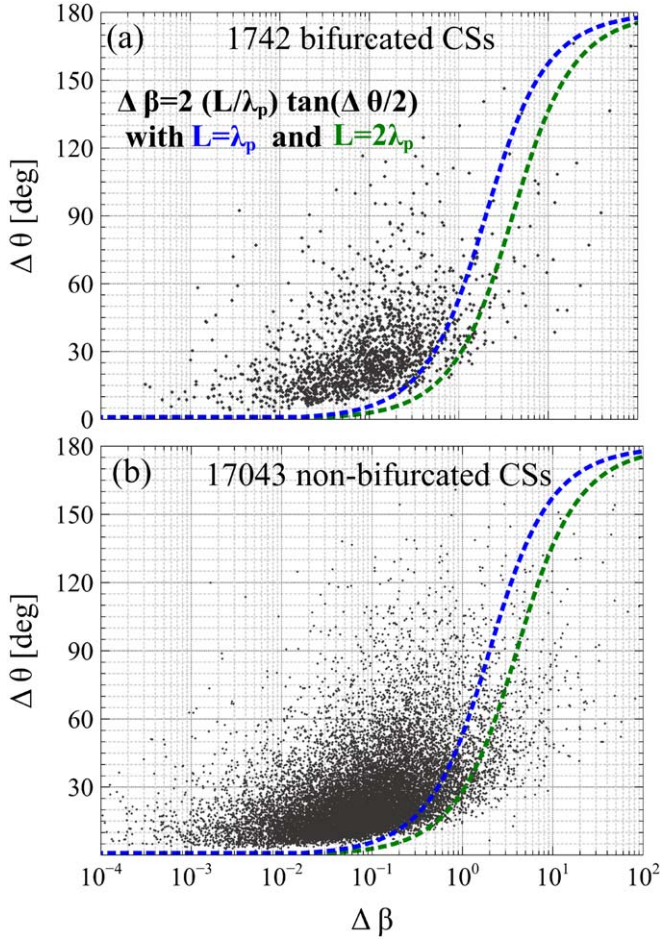


Figure 5. The scatter plots of $\Delta\beta$ vs. $\Delta\theta$ for (a) bifurcated and (b) nonbifurcated CSs. Less than 10% and 3.6% of the CSs violate criterion (1) with $L = \lambda_p$ and $L = 2\lambda_p$, respectively.

Figure 5 presents a test of the diamagnetic suppression condition (1). The scatter plots of $\Delta\beta$ versus $\Delta\theta$ for bifurcated and nonbifurcated CSs are presented in panels (a) and (b). The majority of both bifurcated and nonbifurcated CSs satisfy condition (1) with $L = \lambda_p$. Only 9% of bifurcated CSs and 10% of nonbifurcated CSs violate it. Assuming $L = 2\lambda_p$, we find the condition is violated by only 3.6% of bifurcated CSs and 3.5% of nonbifurcated CSs. The two CSs in Section 2 are actually among those violating condition (1) at both $L = \lambda_p$ and $L = 2\lambda_p$, which occurs because of high local plasma betas (Section 5).

5. Theoretical Interpretation

The asymmetry of solar wind CSs implies that typically, the magnetic field produced by a CS localized in three dimensions is superimposed onto the external magnetic field, $\mathbf{B}_{\text{ext}} = \langle B_x \rangle \mathbf{x} + B_g \mathbf{y}$. The current densities parallel and perpendicular to the external magnetic field are

$$j_{\parallel} = J_x \frac{\langle B_x \rangle}{B_{\text{ext}}} + J_y \frac{B_g}{B_{\text{ext}}}, \quad j_{\perp} = -J_x \frac{B_g}{B_{\text{ext}}} + J_y \frac{\langle B_x \rangle}{B_{\text{ext}}}. \quad (7)$$

The current density should be divergence-free, $\partial j_{\parallel} / \partial l + \partial j_{\perp} / \partial w + \partial j_z / \partial z = 0$, where l is along \mathbf{B}_{ext} , and w is perpendicular to l and CS normal z . Integrating the divergence-free condition

across the CS, we obtain

$$\frac{\partial}{\partial l} \left(\int j_{\parallel} dz \right) + \frac{\partial}{\partial w} \left(\int j_{\perp} dz \right) = 0. \quad (8)$$

Since the magnetic field perturbation should vanish at sufficiently large distances from the localized current density, we obtain the following estimate

$$\int j_{\perp} dz \approx (w/l) \int j_{\parallel} dz, \quad (9)$$

where w and l are the CS width and length, respectively. This equation relates global amplitudes of $\int j_{\parallel} dz$ and $\int j_{\perp} dz$ reached along specific cuts through the three-dimensional CS. For the locally observed quantities, it should be considered a scaling relation valid by the order of magnitude.

The integration of Equation (7) shows that

$$\int j_{\parallel} dz \propto (B_g \Delta B_x - \langle B_x \rangle B_g) / B_{\text{ext}},$$

$$\int j_{\perp} dz \propto (\langle B_x \rangle \Delta B_x + B_g \Delta B_y) / B_{\text{ext}}.$$

Now we note that $|B_g \Delta B_x - \langle B_x \rangle B_g| = |\mathbf{B}_L \times \mathbf{B}_R| = B_L B_R \sin \Delta\theta \approx \langle B \rangle^2 \sin \Delta\theta$, where we took into account that for magnetic fields \mathbf{B}_L and \mathbf{B}_R at the CS boundaries, $B_L B_R \approx \langle B \rangle^2$. We further note that $\langle B_x \rangle \Delta B_x + B_g \Delta B_y$ equals exactly $\Delta(B^2)$, which, in turn, equals $2\langle B \rangle \Delta B$. As a result, Equation (9) allows us to relate the local variation of magnetic field magnitude ΔB with shear angle $\Delta\theta$

$$2\Delta B / \langle B \rangle \approx (w/l) \sin \Delta\theta. \quad (10)$$

In turn, the local pressure balance given by Equation (2) can be approximately written as $2\Delta B / \langle B \rangle \approx \Delta\beta / (1 + \beta)$, which, in combination with Equation (10) reveals that

$$\Delta\beta \approx (1 + \beta)(w/l) \sin \Delta\theta. \quad (11)$$

These theoretical estimates allow several insights into the structure of solar wind CSs. First, Equation (10) naturally explains the correlation between $\Delta B / \langle B \rangle$ and $\Delta\theta$ (Figure 4(b)). Second, it predicts that $\Delta B / \langle B \rangle \ll \Delta\theta$ for CSs with $l \gg w$ and, hence, parallel current density should dominate because $J_{\perp} / J_{\parallel} \approx \Delta B / \langle B \rangle \Delta\theta$ according to Equation (5). The observations indeed show that $\Delta B / \langle B \rangle \Delta\theta \lesssim 0.05$ for more than 95% of the CSs (Figure 4(d)), thereby indicating that solar wind CSs are elongated along the external magnetic field, $l \gg w$. Third, Equation (10) shows that the width-to-length ratio w/l tends to be larger at higher betas because larger values of $\Delta B / \langle B \rangle \Delta\theta$ are typical of higher betas (Figure 4(d)).

Equation (11) shows that condition (1) should always be satisfied provided that

$$L / \lambda_p \gtrsim (1 + \beta) w / l. \quad (12)$$

Three-dimensional turbulence simulations showed that turbulence cascade produces CSs with length l typically one order of magnitude larger than width w , which, in turn, is about one order of magnitude larger than thickness λ (Zhdankin et al. 2013, 2016; Wan et al. 2014; Makwana et al. 2015; Servidio et al. 2015; Franci et al. 2018). Therefore, condition (1) will be automatically satisfied for $L / \lambda_p \gtrsim 0.1 \cdot (1 + \beta)$. Since $\beta \lesssim 10$ for more than 95% of the CSs in our data set as well as at 1 au in general (e.g., Wilson et al. 2018), condition (1) with

$L/\lambda_p = 1$ should be satisfied by most of the solar wind CSs. This is in accordance with our observations (Figure 5). Equation (12) also shows that to satisfy condition (1) at high betas, one needs to assume $L \gg \lambda_p$ because both $(1 + \beta)$ and w/l increase with increasing β . This is exactly the case for the two CSs presented in Section 2, which are observed at high betas and violate condition (1) with $L = \lambda_p$ and $L = 2\lambda_p$.

6. Discussion and Conclusions

We have presented analysis of 18,785 proton kinetic-scale CSs collected in the solar wind using magnetic field measurements at 1/11 s resolution. This is the most extensive data set of kinetic-scale CSs collected at 1 au. We have classified the CSs into nonbifurcated and bifurcated and showed that both types are characterized by similar distributions of asymmetry and magnetic field variation across the CS. The difference is that bifurcated CSs are statistically thicker and magnetic field rotation in them occurs in two steps, in contrast to smooth rotation in nonbifurcated CSs. The only criterion in our visual identification of bifurcated CSs was a temporal profile of dB_x/dt with two well-separated peaks so that the larger thickness of bifurcated CSs is a realistic property rather than a trivial consequence of the visual classification. The magnetic field magnitude does not strongly vary across the CSs, which is consistent with previous studies of larger-scale CSs (Burlaga et al. 1977; Lepping & Behannon 1986; Vasquez et al. 2007). The magnetic field variation across the CSs is dominated by rotation and, accordingly, the current density in solar wind CSs is statistically dominated by the parallel component, $J_{\perp}/J_{\parallel} \ll 1$. Nevertheless, the magnetic field variation across solar wind CSs is noticeable and can be rather large at high betas. We have shown theoretically that magnetic field variation across solar wind CSs is proportional to the width-to-length ratio. Based on that, we have concluded that solar wind CSs are elongated along an external magnetic field (length is much larger than width), and larger width-to-length ratios tend to occur at higher plasma betas. The CS elongation along the external magnetic field is consistent with the results of turbulence simulations (Servidio et al. 2011, 2015; Zhdankin et al. 2013, 2016; Wan et al. 2014; Makwana et al. 2015; Franci et al. 2018; Pezzi et al. 2021), while the beta dependence of the CS geometry would be worth testing in future simulations.





The variation of the magnetic field magnitude between the CS boundaries corresponds to plasma beta variation, which is a crucial quantity in the theory of diamagnetic suppression of magnetic reconnection (Swisdak et al. 2010). Because the magnetic field is typically not stable over 3–9 s at the boundaries of the CSs in our data set, the plasma measurements at the boundaries could not be used to obtain precise estimates of plasma beta variation across the CSs. Instead, we obtained an approximate estimate of the plasma beta variation using a few points of plasma measurements around a CS and Equation (2) based on the assumption that there is a pressure balance across the CS. Note though, that the use of plasma beta variations obtained using particle measurements 9 s before and after each CS would not change our conclusions about diamagnetic suppression of magnetic reconnection in the solar wind.

The idea that magnetic reconnection in asymmetric CSs typically produced by a turbulence cascade can provide substantial contribution to plasma heating and affect turbulence

cascade development has been suggested based on various turbulence simulations (Matthaeus & Lamkin 1986; Servidio et al. 2009, 2011, 2015; Franci et al. 2018). However, still the critical question in the solar wind physics is how often reconnection occurs at proton kinetic scales and why it is relatively rare according to plasma measurements at 3 s cadence or ≈ 1000 km spatial resolution (e.g., Gosling 2012; Osman et al. 2014). Phan et al. (2010, 2020) and Gosling & Phan (2013) showed that reconnection exhausts satisfy the condition necessary for reconnection to occur (Swisdak et al. 2003, 2010), which could create an impression that it controls reconnection onset in the solar wind, although a few tens of nonreconnecting CSs have been found to satisfy that condition as well (Phan et al. 2020). In this Letter we have shown that almost all kinetic-scale CSs in the solar wind satisfy condition (1). Since reconnection is probably occurring in only a small subset of solar wind CSs, this means that condition (1) is satisfied regardless of the presence or absence of reconnection. In fact, we have shown this condition is satisfied by the majority of solar wind CSs due to their geometry dictated by the source, which is the local plasma turbulence (Matthaeus & Lamkin 1986; Vasquez et al. 2007; Greco et al. 2009, 2016; Zhdankin et al. 2012). In conclusion, we have demonstrated that reconnection in the solar wind cannot be suppressed or controlled by the diamagnetic suppression condition and should be determined by some other current sheet properties.

The work of I.V. and T.P. was supported by NASA's Living With a Star grant #80NSSC20K1781. The work of A.A. was supported by NASA's Living With a Star grant #80NSSC20K1788. The work of K.A. was supported by National Science Foundation grant No. 1902684. I.V. thanks Ajay Lotekar and Rachel Wang for discussions. The data used in the analysis are publicly available at <https://cdaweb.gsfc.nasa.gov/pub/data/wind/>.

ORCID iDs

I. Y. Vasko  <https://orcid.org/0000-0002-4974-4786>
 T. D. Phan  <https://orcid.org/0000-0002-6924-9408>
 S. D. Bale  <https://orcid.org/0000-0002-1989-3596>
 F. S. Mozer  <https://orcid.org/0000-0002-2011-8140>

References

- Artemyev, A. V., Angelopoulos, V., Vasko, I. Y., et al. 2019, *GeoRL*, **46**, 1185
 Burlaga, L. F., Lemaire, J. F., & Turner, J. M. 1977, *JGR*, **82**, 3191
 Cassak, P. A., Drake, J. F., & Shay, M. A. 2006, *ApJL*, **644**, L145
 Chasapis, A., Matthaeus, W. H., Parashar, T. N., et al. 2017, *ApJL*, **844**, L9
 Cranmer, S. R., Gibson, S. E., & Riley, P. 2017, *SSRv*, **212**, 1345
 EnŽl, J., Přeč, L., Šafránková, J., & Němeček, Z. 2014, *ApJ*, **796**, 21
 Franci, L., Landi, S., Verdini, A., Matteini, L., & Hellinger, P. 2018, *ApJ*, **853**, 26
 Gosling, J. T. 2007, *ApJL*, **671**, L73
 Gosling, J. T. 2012, *SSRv*, **172**, 187
 Gosling, J. T., & Phan, T. D. 2013, *ApJL*, **763**, L39
 Gosling, J. T., Phan, T. D., Lin, R. P., & Szabo, A. 2007, *GeoRL*, **34**, L15110
 Gosling, J. T., Skoug, R. M., McComas, D. J., & Smith, C. W. 2005, *JGRA*, **110**, A01107
 Gosling, J. T., & Szabo, A. 2008, *JGRA*, **113**, A10103
 Greco, A., Matthaeus, W. H., Perri, S., et al. 2018, *SSRv*, **214**, 1
 Greco, A., Matthaeus, W. H., Servidio, S., Chuychai, P., & Dmitruk, P. 2009, *ApJL*, **691**, L111
 Greco, A., Perri, S., Servidio, S., Yordanova, E., & Veltri, P. 2016, *ApJL*, **823**, L39
 Horbury, T. S., Burgess, D., Fränz, M., & Owen, C. J. 2001, *GeoRL*, **28**, 677

- Knetter, T., Neubauer, F. M., Horbury, T., & Balogh, A. 2004, *JGRA*, **109**, [A06102](#)
- Lepping, R. P., Acuña, M. H., Burlaga, L. F., et al. 1995, *SSRv*, **71**, 207
- Lepping, R. P., & Behannon, K. W. 1986, *JGR*, **91**, 8725
- Lin, R. P., Anderson, K. A., Ashford, S., et al. 1995, *SSRv*, **71**, 125
- Makwana, K. D., Zhdankin, V., Li, H., Daughton, W., & Cattaneo, F. 2015, *PhPI*, **22**, 042902
- Matthaeus, W. H., Dasso, S., Weygand, J. M., et al. 2005, *PhRvL*, **95**, 231101
- Matthaeus, W. H., & Lamkin, S. L. 1986, *PhFI*, **29**, 2513
- Mistry, R., Eastwood, J. P., Phan, T. D., & Hietala, H. 2017, *JGRA*, **122**, 5895
- Neugebauer, M. 2006, *JGRA*, **111**, A04103
- Newbury, J. A., Russell, C. T., Phillips, J. L., & Gary, S. P. 1998, *JGR*, **103**, 9553
- Ogilvie, K. W., Chornay, D. J., Fritzenreiter, R. J., et al. 1995, *SSRv*, **71**, 55
- Osman, K. T., Matthaeus, W. H., Gosling, J. T., et al. 2014, *PhRvL*, **112**, 215002
- Osman, K. T., Matthaeus, W. H., Greco, A., & Servidio, S. 2011, *ApJL*, **727**, L11
- Pezzi, O., Pecora, F., Le Roux, J., et al. 2021, *SSRv*, **217**, 39
- Phan, T. D., Bale, S. D., Eastwood, J. P., et al. 2020, *ApJS*, **246**, 34
- Phan, T. D., Gosling, J. T., Davis, M. S., et al. 2006, *Natur*, **439**, 175
- Phan, T. D., Gosling, J. T., Paschmann, G., et al. 2010, *ApJL*, **719**, L199
- Phan, T. D., Paschmann, G., Gosling, J. T., et al. 2013, *GeoRL*, **40**, 11
- Pulupa, M. P., Salem, C., Phan, T. D., Gosling, J. T., & Bale, S. D. 2014, *ApJL*, **791**, L17
- Sonnerup, B. U. Ö., & Scheible, M. 1998, *ISSIR*, **1**, 185
- Servidio, S., Greco, A., Matthaeus, W. H., Osman, K. T., & Dmitruk, P. 2011, *JGRA*, **116**, A09102
- Servidio, S., Matthaeus, W. H., Shay, M. A., Cassak, P. A., & Dmitruk, P. 2009, *PhRvL*, **102**, 115003
- Servidio, S., Valentini, F., Perrone, D., et al. 2015, *JPIPh*, **81**, 325810107
- Sorriso-Valvo, L., Carbone, V., Veltri, P., Consolini, G., & Bruno, R. 1999, *GeoRL*, **26**, 1801
- Swisdak, M., Opher, M., Drake, J. F., & Alouani Bibi, F. 2010, *ApJ*, **710**, 1769
- Swisdak, M., Rogers, B. N., Drake, J. F., & Shay, M. A. 2003, *JGRA*, **108**, 1218
- Tsurutani, B. T., & Smith, E. J. 1979, *JGR*, **84**, 2773
- Vasquez, B. J., Abramenko, V. I., Haggerty, D. K., & Smith, C. W. 2007, *JGRA*, **112**, A11102
- Wan, M., Rappazzo, A. F., Matthaeus, W. H., Servidio, S., & Oughton, S. 2014, *ApJ*, **797**, 63
- Wilson, L. B., III, Stevens, M. L., Kasper, J. C., et al. 2018, *ApJS*, **236**, 41
- Wu, P., Perri, S., Osman, K., et al. 2013, *ApJL*, **763**, L30
- Zhdankin, V., Boldyrev, S., & Mason, J. 2012, *ApJL*, **760**, L22
- Zhdankin, V., Boldyrev, S., & Uzdensky, D. A. 2016, *PhPI*, **23**, 055705
- Zhdankin, V., Uzdensky, D. A., Perez, J. C., & Boldyrev, S. 2013, *ApJ*, **771**, 124